The structure of atomically dispersed Pt in a SnO_2 thin film under reaction conditions – Origin of its high performance in MEMS gas sensor catalysis

Naoyoshi Murata[1], Takuya Suzuki[1], Yunli Lin [2], Hiroaki Nitani[3], Yasuhiro Niwa[3], Takahiro Wada[4], Motohiro Uo[4] and Kiyotaka Asakura*[2]

1. *Corporate R & D Headquarters, Fuji Electric Co., Ltd., Tokyo 191-8502, Japan*
2. *Institute for Catalysis, Hokkaido University, Sapporo 001-0021, Japan*
3. *Photon Factory, Institute of Structure Material Science, High Energy Accelerator Research Organization (KEK-PF), Oho 1-1, Tsukuba 305-0811, Japan*
4. *Graduate School of Medical and Dental Sciences, Tokyo Medical and Dental University, Yushima 1-5-45, Bunkyo-ku, Tokyo 113-8549, Japan*

Abstract

A battery-driven micro electromechanical systems (MEMS) gas sensor has been developed for household safety when using natural gas. The heart of the MEMS gas sensor is a 7.5 at% Pt–SnO_2 thin film catalyst deposited on the SnO_2 sensor layer. The catalyst enhances the sensitivity to methane, though its structure under the working conditions is unclear. In this study, *in situ* XAFS was applied to a 7.5 at% Pt–SnO_2 catalyst layer deposited on a Si substrate, and we demonstrated that atomically dispersed Pt maintains its lattice position in SnO_2 with a small loss of surrounding lattice oxygen in the presence of 1% CH_4 and a more reducing gas of 1% H_2 at the reaction temperature (703 K), *i.e.,* no Pt aggregation is observed. The lost oxygen is easily recovered by re-oxidation by air. This work has revealed that the atomically dispersed Pt in the SnO_2 lattice is the active structure and it is stable even under reaction conditions, which guarantees a long lifetime for the gas sensor.

Keywords

in situ XAFS, Pt–SnO_2, Solid-state, Reducing gas, Micro gas sensor

E-mail: askr@cat.hokudai.ac.jp

1. Introduction

The demand for natural gas is increasing because of the easy supply and its eco-friendliness as an energy source.[1] However, safety issues prevent further utilization of natural gas.[2] The main ingredient of natural gas is methane, whose lower explosion limit is 5.3% or 53000 ppm in air. In 2010, 665 cases of methane gas leakage were reported in Japan, 60% of which took place at residential locations.[3] A semiconductor-type gas sensor was studied by Seiyama et al. in the 1960s.[4,5] The SnO_2 n-type semiconductor gas sensor which was developed by Taguchi et al.[6] is now widely used since its conductivity varies with partial pressure of the reductive gases.[7,8] Since the SnO_2 sensor requires a high operation temperature for the reaction between SnO_2 and the gas, a continuous external power supply is necessary to heat the sensor. In order to increase the number of home-use gas sensors, battery-driven or wireless models are important for their good appearance and their easy installation. For this purpose, low power consuming sensors have to be developed with a high sensitivity and a lifetime longer than 5 years.

From this standpoint, Suzuki et al. have developed a new type of gas sensor using MEMS (micro electromechanical systems) technology.[9-15] This MEMS gas sensor has a multi-layer structure of "Pd–Al_2O_3 thick film catalyst layer/Pt–SnO_2 thin film catalyst layer/SnO_2 thin film sensor layer/Pt electrode/thin film heater" as shown in Fig. S1(c).[15] The sensor can detect methane at 12500 ppm, which is 1/4 of the methane explosion limit, even after 5 years. The Pd–Al_2O_3 thick film layer enhances the selectivity towards methane. The Pt–SnO_2 provides high sensitivity towards methane gas. The SnO_2 thin film sensor layer changes its conductivity according to the CH_4 concentration.

There are two possible structures of Pt to enhance methane sensitivity in Pt–SnO_2. One involves Pt ions located at SnO_2 lattice sites. The redox of Pt ions enhances the SnO_2 response for the electrical conductivity for reducing gases (methane). The other is Pt nanoparticles on SnO_2. Metallic Pt nanoparticles activate methane and oxygen to supply them to the SnO_2. Yamazoe and Kocemba et al. proposed a spillover mechanism where the Pt nanoparticles on the SnO_2 surface improved the performance of SnO_2 as a gas sensor.[16-18] This was consistent with previous reports that oxidized Pt in addition to Pt aggregates were found in SnO_2 substrates depending on

the atmosphere and Pt concentration.[7,19-23] DFT calculations showed that the lattice oxygen near Pt metal particles actively worked for the redox reaction.[24]

On the other hand, in our previous characterizations using XRD, XPS and XAFS, we found that Pt was present in the SnO_2 lattice and occupied Sn sites.[25] We inferred that atomically dispersed Pt in SnO_2 showed high performance. This result was consistent with Weimer's reports where they found Pt ions were located at Sn positions in the rutile structure on Pt–SnO_2.[20,26,27] The novelty of our Pt–SnO_2 was the higher Pt concentration. They prepared a Pt content as low as 0.2 wt%, while our Pt–SnO_2 contained about 29 wt% ($Pt_{0.075}Sn_{0.255}O_{0.660}$), where Pt was stably located in the SnO_2 lattice, and we did not find Pt particles.

Criticisms have arisen regarding our catalyst in that such high Pt loading is not stable in the SnO_2 lattice under real reaction conditions, may leave the lattice to form metallic Pt clusters and the Pt clusters can collapse to return to the lattice after the reaction, as in Pd perovskite catalysts that showed the formation and the redispersion of Pd nanoparticles in Pd perovskite catalyst under reaction conditions.[28] It is important to determine the real structure under reaction conditions. The difficulty is that the system contains a very small total amount of Pt in the Pt–SnO_2 thin layer on the flat Si substrate. We applied *in situ* fluorescence EXAFS and developed a new *in situ* reaction cell.[29] We obtained a good S/N ratio for the *in situ* Pt L_3-edge EXAFS signal under reducing gas at high temperature using the *in situ* cell that allows us to detect the fluorescence signal with a large half-cone angle (56°). We can carry out data analysis using difference spectra to elucidate minute changes in EXAFS oscillations during reactions. In this study, we analyzed the EXAFS data during the reaction and demonstrated the stability of Pt–SnO_2 in the lattice of the rutile structure during the reduction reaction even after the partial loss of surrounding oxygen atoms around Pt. We discuss the enhancement mechanism of Pt–SnO_2 for methane sensitivity.

2. Experimental

2.1. Sample preparation

The 400 nm thick Pt–SnO_2 thin layers were prepared on Si substrates covered with native SiO_2 film (600 nm) using a sputter-deposition method.[25]

Pt concentration in the film was 7.5 at% ($Pt_{0.075}Sn_{0.255}O_{0.660}$ (= $Pt_{0.227}Sn_{0.773}O_2$)) and 14.0 at% ($Pt_{0.140}Sn_{0.190}O_{0.660}$) determined by inductively coupled plasma mass spectrometry (ICP-MS, SPS3100 of Hitachi High-Tech Science Corporation).

2.2. Characterization of the catalyst

XRD (X-ray diffraction) patterns were recorded by using RIGAKU ATX-G at 50 kV and 300 mA (Cu Kα from $\lambda = 1.5418$ Å). Lattice spacings were obtained by $d_{hkl} = \lambda/(2\,sin(\theta_{hkl}))$. Lattice constants, a and c, were obtained by least square fitting using $1/d_{hkl}^2 = (h^2 + k^2)/a^2 + l^2/c^2$ assuming a rutile structure.

Pt L_3-edge XAFS spectra were measured at BL-12C of KEK-PF (Photon Factory, Institute of Structure Materials Science, High Energy Accelerator Research Organization; 2.5 GeV- 500 mA) using a Si(111) double crystal monochromator.[30,31] The Sn K-edge XAFS spectra were measured at the NW-10A of KEK-PF-AR equipped with a Si(311) monochromator.[32] The *in situ* XAFS was measured in a fluorescence mode using an *in situ* fluorescence XAFS measurement cell described elsewhere.[29] XAFS spectra were analyzed with REX2000 (Ver. 2.5, RIGAKU).[3335] The background was removed by a spline smoothing method with Cook and Sayers criteria.[36] The k^3-weighted EXAFS (Extended X-ray Absorption Fine Structure) oscillations were Fourier-transformed to k-space over $k = 3.0 - 13.8$ Å for Pt L_3-edge spectra, and over $k = 3.0 - 14.0$ Å for Sn K-edge in the *in situ* measurement cell. Each peak in the Fourier transform was filtered and inversely Fourier-transformed to the k-space for the curve fitting analysis. We carried out non-linear least square curve fitting using the following equations:

$$k^3\chi(k) = \sum_j S_0^{\,2}\frac{k^2 N_j F_j(k)}{r_j^{\,2}} e^{-2k^2\sigma_j^{\,2}} e^{-\frac{2r_j}{\lambda_j}} \sin(2kr_j + \phi_j)$$
$$k = \sqrt{\frac{2m}{\hbar^2}(h\nu - E_o - \Delta E)} \quad , \qquad (1)$$

where S_0^2, N_j, r_j, and σ_j were the amplitude reduction factor, the coordination number, the bond distance, and the Debye Waller (DW) factor, of the j-th coordination shell, respectively. λ_j was the mean free path. $F_j(k)$

and $\phi_j(k)$ were the backscattering amplitude and phase-shift functions for the *j-th* shell which were obtained from FEFF (ver. 8.0).[37-39] E_0 was the absorption edge energy and was tentatively determined as the inflection points. It was corrected by the energy shift, ΔE, during the fitting process. The errors were estimated by Hamilton test for the R-factor determined by the curve fitting procedure. The significance level was more than 90%.[40]

For the *in situ* XAFS measurement, a 1 cm^2 sample was loaded in the cell and heated to 703 K with a ramping rate of 100 K/min.[29] Experiments were carried out in seven steps. First, the sample was heated to 703 K after XAFS measurement in dry air of 200 mL/min flow. In the next step, the cell was filled with the 1% CH_4 gas (dry air balance) at the same flow rate. The flow gas was then changed to dry air followed by measurement in the 1% H_2 gas (dry air balance) flow. Finally, the sample was treated under dry air again for 1 hour at 703 K and was cooled to room temperature (RT). XAFS measurements were carried out on all steps 15 min after the gas replacements. Difference spectra were taken directly between the ones before and during the reaction conditions. Phase-corrected Fourier transforms on the difference spectra were applied to confirm visually whether the change was due to oxygen loss or gain.[41]

3. Results and discussion

3.1. Brief summaries on the sensor properties and the Pt–SnO_2 local structure under the ambient conditions

The details about the sensor properties and the analysis of the local structures around Pt and Sn under static conditions before the reaction were described in the previous literature.[9-15,25] We described briefly the additional information.

Figure S1(a) shows the response curve of the conductivity under the atmosphere of the 4000 ppm CH_4.[9] The sample temperature was increased by applying power to the heater. The equilibrium conductance was attained at 40 ms. Thus the heating pulse width was 100 ms followed by a 60 s interval. Figure S1(b) shows the sensitivity of CH_4 and H_2. At high temperature, a high sensitivity of CH_4 is achieved. The H_2 and other organic compounds were removed by Pd/Al_2O_3 overlayer where Pd was in

the state of PdO.[9,11,42 43]

XRD, XAFS and XPS results in the previous paper showed that the Pt–SnO_2 took the rutile structure and the Pt was located at the position of Sn in the SnO_2 lattice.

Figure 1 shows a typical XRD pattern of 7.5 at% Pt–SnO_2 thin film on Si substrate with the reference of SnO_2 film The Pt–SnO_2 thin film has a rutile structure giving peaks at 26.72, 33.93, 38.30 and 52.16°, corresponding to (110), (101), (200) and (211) of the structure of SnO_2. The SnO_2 and Pt–SnO_2 films gave a stronger (101) peak, indicating preferential orientation of the SnO_2 films. The lattice constants of 7.5 at% Pt–SnO_2 is 4.71 Å for the a-axis and 3.19 Å for the c-axis, a little shorter than those of SnO_2 thin film (4.748 Å of a-axis and 3.195 Å of c-axis). Addition of Pt makes the rutile lattice constant a little smaller (less than 1%). No other peaks corresponding to Pt metal are found.[25]

Figures 2a and 2b show the k^3-weighted Sn K-edge EXAFS oscillations ($k^3\chi(k)$) and the Fourier transforms (FT) for 7.5 at% and 14.0 at% Pt–SnO_2 samples in dry air at RT together with several reference samples, respectively. The FT pattern of 7.5 at% Pt–SnO_2 in dry air at RT is close to that of SnO_2. The first peak at 1 – 2 and the peaks at 2.5 – 4 Å of Sn K-edge correspond to Sn–O and Sn–M (M = Pt, Sn) bonds in the rutile structure, respectively. The FT peak intensity at 2.5 – 4 Å decreases to half due to the interference of Sn–Pt and Sn–Sn interactions. The oscillation intensity of 14.0 at% Pt–SnO_2, on the other hand, greatly decreases compared to that of 7.5 at%, and especially, peaks at 2.5 – 4 Å are lost in the FT, indicating the amorphous structure of 14.0 at% Pt–SnO_2 as shown in a previous paper.[25]

Figure 3a and 3b show the Pt L_3-edge $k^3\chi(k)$ and FTs for 7.5 at% and 14.0 at% Pt–SnO_2 samples in dry air at RT with reference compounds, respectively. The Pt L_3-edge $k^3\chi(k)$ oscillations and FT of 7.5 at% Pt–SnO_2 have different oscillations from those of Pt foil, PtSn and PtO_2, which indicates the structure of Pt in Pt–SnO_2 is not the structure of these reference compounds. Three peaks appear at 2.5–4 Å in Pt–SnO_2. Figure S2 shows the Pt L_3-edge and Sn K-edge oscillations. Since L_3-edge oscillation is π rad different from that of K-edge, the Pt L_3-edge is multiplied by –1. The two oscillations agree with each other, confirming Pt is located at the substitution site of Sn in the SnO_2 lattice. The oscillation intensity of 14.0 at% Pt–SnO_2 tremendously decreases and has no peaks around 3 Å.

Pt–SnO_2 has an amorphous-like state.

Curve fitting analyses are tabulated in Tables 1-3. The Sn–O bond is found at coordination number (CN) = 6.0 (±0.2), r = 2.05 Å and the Pt–O bond at CN = 6.0 (±0.3), r = 2.01 Å in Pt–SnO_2.

The higher shell peaks in the range of 2.5 – 4 Å consist of two components of the Sn–Sn(Pt) in the SnO_2 lattice. To confirm the Pt is randomly distributed in the SnO_2, curve fitting analyses in the second and the third shells are carried out as shown in SI-3. The coordination numbers around Pt and Sn at the corresponding shells agree within the error bar, indicating the Pt is randomly distributed in the SnO_2 bulk but not located at the surface.

3.2. *In situ* EXAFS of Pt–SnO_2 under different gases

Figures 4a and 4b show the k^3-weighted Sn K-edge EXAFS oscillations ($k^3\chi(k)$) and the FTs for SnO_2 under different gas flow conditions at 703 K. The change of the EXAFS oscillations and their FTs of Sn K-edge in CH_4 and H_2 is little. Table 1 shows the curve fitting analysis of Sn K-edge.

Figures 5a and 5b show the k^3-weighted Sn K-edge EXAFS oscillations ($k^3\chi(k)$) and the FTs for 7.5 at% Pt–SnO_2 under various gas flows at 703 K. The fitting results are summarized in Table 2 for Sn–O bonding. The Sn K-edge EXAFS oscillations and their FTs of Sn in CH_4 and H_2 showed little change from the dry air.

Figures 6a and 6b show the k^3-weighted Pt L_3-edge EXAFS oscillations ($k^3\chi(k)$) and the FTs for 7.5 at% Pt–SnO_2 under different conditions at 703 K. Table 3 shows the curve fitting results for Pt–O bonding. The oscillations and FTs in the CH_4 flow and H_2 flow show a little change in the EXAFS oscillation compared to those of the dry air.

In order to confirm the change more clearly, we calculated the difference EXAFS ($k^3\triangle\chi(k) = k^3\chi(k)_{after} - k^3\chi(k)_{before}$) before and after contact with H_2 at 703 K as shown in Fig. 7a. Figure 7b shows the Fourier transform of the difference spectrum. A peak appears at 1.5 Å in the absolute value of FT, indicating the oscillation change is related to Pt–O. We are not able to find the Pt–Pt related peak around 2.3 Å, indicating that the Pt nanocluster is rarely formed even after the H_2 treatment. Since the absolute part of the FT does not include phase information, it does not necessarily mean the FT peak in the absolute part of the difference spectrum due to the increase in

the Pt–O bond. In the phase-corrected FT, the imaginary and absolute parts give the peak for the Pt–O at the real bond distance. If the positive imaginary peak appears, the Pt–O increases and vice versa. Figure 8 shows imaginary and absolute parts of the phase-corrected Fourier transform of the difference spectrum of Pt–SnO_2 over the *k* range 2 – 9 Å. The imaginary part gives a negative peak at the peak in the absolute part around 2 Å. Therefore, we conclude that the change at 1 – 2 Å in FT during H_2 reaction indicates the decrease of the Pt–O peak. Table 3 shows the curve fitting results where the coordination number of Pt–O after the treatment at 703 K decreases though the bond distance is invariant. We have concluded that after the H_2 treatment, the Pt–O bond is cleaved and no Pt–Pt formation occurs. Although the decrease in Sn–O coordination seems to occur after the H_2 treatment, the Pt–O decrease is more, indicating that O is removed mainly from Pt–O–Pt bonds.

3.3. Sn K-edge and Pt L_3-edge XANES

Figure 9 shows the Sn K-edge and Pt L_3-edge XANES (X-ray Absorption Near Edge Structure) for SnO_2 and for Pt–SnO_2. The Sn K-edge XANES for Pt–SnO_2 shows the typical features of SnO_2. Little change is found in the Sn K-edge in the SnO_2 film. On the other hand, a little change in the Sn K-edge of Pt–SnO_2 is found in CH_4 and in H_2 flows where the first edge peak intensities are reduced, indicating the Sn is partially reduced. A small decrease also occurs in the white line of Pt L_3-edge XANES of Pt–SnO_2 under the flow of CH_4, which is enhanced under the H_2 flow, indicating the Pt valence state is decreased. The H_2 flow gives a relatively large reduction of the white line peak. The amount of XANES changes qualitatively corresponds to the change of the Pt–O and Sn–O coordination numbers. The reduction of the first main peaks in both Sn K-edge and Pt L_3-edge is caused by the loss of O.

4. Discussion

4.1. Structural stability of Pt–SnO_2

Our previous EXAFS measurements have demonstrated that Pt is located at the lattice (substitution) site of Pt–SnO_2 at RT.[25] The present work indicates that the Pt is homogeneously and randomly distributed in the SnO_2 lattice. The local structure around Pt is a little more compressed than

that around SnO_2, judging from the shorter Pt–O, Pt–Sn and Pt–Pt distances, corresponding well to the X-ray diffraction results that the lattice constants of Pt–SnO_2 are smaller than those of the corresponding SnO_2.

To confirm that Pt is not released from the lattice during the reaction conditions to form Pt nanoparticles, we carried out *in situ* EXAFS under the reaction conditions and difference spectra analysis. No Pt nanoparticles are found even in the presence of 1% H_2 at high temperature, which is a much more severe reduction condition than the real operation conditions. Thus, the enhancement in the CH_4 gas detection is not due to Pt nanoclusters. Though Pt metal is easily formed under reductive conditions,[4446] relatively oxidative conditions (1% H_2 and CH_4 in dry air) keep the stable Pt single atom dispersion in the lattice.

Under the interaction of CH_4 or H_2, the sensor response against these gases occurs with the loss of the oxygen around Pt, while keeping its location at the lattice of SnO_2. Suzuki et al. reported that the introduction of a Pt–SnO_2 thin film in a MEMS sensor realized long-term stability of sensor activity.[14] The long lifetime is due to the stable structure of the Pt atoms in the lattice under the working conditions. In the reduction process with H_2, more oxygen around Pt is removed than around Sn. This is due to the weaker Pt–O bond compared to Sn–O. The fact that Pt metal nanoparticles are not created suggests that not only the surface Pt–O but also the bulk Pt–O is lost because Pt nanoclusters would be formed if only the surface Pt–O were removed. The oxygen atoms are supplied by diffusion from the bulk Pt–SnO_2 to the surface as well as from the gas phase O_2.

4.2. Structure and activity

Pt–SnO_2 enhances the sensor sensitivity by increasing the resistance in the SnO_2 thin film sensor device as shown in Figs. S1(a) and (b).[9,25] In this *in situ* XAFS work, we confirmed that the active structure is Pt atoms in the SnO_2 lattice, not Pt metal particles produced during the gas reaction. Recently, these Pt single atom catalysts have drawn much interest[47] for the CO oxidation reaction [48] - [51] NO oxidation, [52] propane oxidation, [53] formaldehyde oxidation, [54] electrochemistry, [55, 56] CO_2 reduction [57, 58] and hydrosilylation.[59] The high redox activity of Pt is the origin for the high performance of Pt single atom catalysts. Weimar et al. claimed that Pt atomically dispersed in the SnO_2 matrix was the active structure, which

generated atom/molecular adsorption sites for oxygen near the Pt atoms at the surface.[20,26,27] The easy loss and gain of oxygen in the Pt–SnO_2 layer can control the oxygen content in the SnO_2 thin film sensor layer discussed below.

4.3. Mechanism to enhance the sensitivity towards reducing gases by the Pt-SnO_2 overlayer

The sensing mechanism for SnO_2 is usually understood as follows. SnO_2 is known as an n-type semiconductor so that the carriers are electrons. When the O_2 is chemisorbed on the surface of SnO_2, the number of electron carriers decreases due to the chemisorbed oxygen. When reducing gases such as H_2 and CH_4 are introduced to the surface, the chemisorbed oxygen is removed and trapped electrons are liberated to increase the number of electron carriers in SnO_2. Table 4 summarizes the role and structure of Pt in Pt-SnO_2 in the previous literature and this paper. In many studies, metallic or oxidized Pt nanoparticles were active sites. In contrast, we have found the Pt is located in the SnO_2 lattice even at high Pt loading.

The enhancement effect of Pt was discussed in the spillover model of activated species by Pt. Hydrogen or other reducing components were activated on the Pt surface and diffused to the SnO_2 surface where adsorbed oxygen was reacted and removed to increase the conductivity.

We propose three possibilities for the enhancement effect of the Pt–SnO_2 layer.

1. The Pt–SnO_2 layer activates the reducing gases through dissociative adsorption and the activated species spill over on the Pt–SnO_2 surface to the SnO_2 sensor layer in a similar way to the previous report.[16]
2. The loss of oxygen in the Pt–SnO_2 layer modifies the SnO_2 electronic state by changing the thickness of the space-charge layer.[16]
3. Pt enhances the CH_4 and lattice oxygen reaction to create oxygen defects which diffuse through the Pt–SnO_2 layer to the SnO_2 sensor layer.

The first mechanism is less plausible because the activated species on the Pt–SnO_2 surface react easily during surface diffusion with O_2 on the active Pt–SnO_2 layer. The second mechanism is also less possible because the space-charge layer thickness in the SnO_2 sensor layer is mainly affected by the interface between the Pt–SnO_2 and the SnO_2 and most of the Pt–SnO_2

does not act to control the thickness of the space-charge layer. In the third mechanism, oxygen-defect diffusion can be accelerated by the presence of Pt due to the weaker Pt–O bonding. Since Pt–SnO_2 is directly deposited on the SnO_2 thin film sensor layer and both have the same rutile lattices with a small lattice mismatch of less than 1%, the diffusion of oxygen atoms from/to the SnO_2 film sensor layer to/from the Pt–SnO_2 lattice occurs smoothly through the junction of the Pt–SnO_2 and SnO_2. The driving force for the diffusion of oxygen over the junction between the two phases (Pt–SnO_2 and SnO_2) is the difference in the chemical potential of oxygen as found in the $VSbO_4$–Sb_2O_4 system.[60] The loss of oxygen in the SnO_2 sensor layer leaves extra carrier electrons. When the reducing gases disappear, the Pt in Pt–SnO_2 is easily oxidized to refill the defects and supply oxygen atoms to the SnO_2 sensor layer to reduce the carrier density (free electron density). Such easy loss and gain of oxygen atoms around Pt atoms and their rapid diffusion to the SnO_2 layer is the origin for the high activity and high response of the MEMS sensor. The stability of atomically dispersed Pt in the SnO_2 lattice gives rise to its long lifetime.

5. Conclusion

The local structure during CH_4 and H_2 gas oxidation of a 7.5 at% Pt–SnO_2 catalyst prepared by a sputter-deposition technique was investigated to evaluate the advantages of this catalyst for application as a gas sensor. *In situ* XAFS measurements revealed that Pt atoms randomly located in the SnO_2 lattice are partially reduced to lose the surrounding oxygen while keeping their lattice position under reducing gases of 1% CH_4 and 1% H_2. No Pt metal nanoparticles were observed even during the reaction. The oxygen defects around Pt created by the reaction with reducing gases diffuse into the Pt–SnO_2 bulk and further into the SnO_2 sensor layer. When the reducing gas flow is stopped, the Pt atoms are oxidized and supply oxygen atoms in a reverse manner to the SnO_2 sensor layer. This easy creation and diffusion of defects or oxygen atoms around Pt atoms is the origin of the high sensitivity of the Pt–SnO_2 MEMS sensor. The stable Pt atoms in the lattice are responsible for the long lifetime of the sensor and guarantee a 5-year battery-driven sensor.

6. Further information is available in the Supporting Information (SI). The following are the contents.

1. Gas response properties of the sensor
2. Pt L_3- and Sn K-edge EXAFS oscillations in Pt-SnO_2
3. Second and the third shell analysis of Pt-SnO_2

7. Acknowledgement

This work is partially supported by a Grant-in-Aid for Scientific Research A, 20H00367.

8. References.

[1] United Nations (UN), *2010 Energy Statistics Yearbook.* United Nations, New York, 2014.

[2] National Transportation Safety Board, Natural Gas-Fueled Building Explosion and Resulting Fire, New York City, New York, March 12, 2014. Pipe-line Accident Report NTSB/PAR-15/01, (2015).

[3] Fire and Disaster Management Agency of Japan, *Statistical Table for explosion and leakage cases by gases and hazardous chemicals in 2011,* 2011

[4] Seiyama, T.; Kato, A.; Fujiishi, K.; Nagatani, M. A New Detector for Gaseous Components using Semiconductive Thin Films. *Anal. Chem.* **1962**, *34*, 1502-1503.

[5] Seiyama, T.; Kagawa, S. Study on a Detector for Gaseous Components Using Semiconductive Thin Films. *Anal. Chem.* **1966**, *38*, 1069-1073.

[6] Taguchi, N. Gas Detecting Device United States Patent 3,631, 436, July 4th, **1970**.

[7] Heiland, G. Homogeneous Semiconducting Gas Sensors. *Sens. Actuators* **1981-1982**, *2*, 343-361.

[8] Barsan, N.; Koziej, D.; Weimar, U. Metal oxide-based gas sensor research: How to? *Sens. Actuators B: Chem.* **2007**, *121*, 18-35.

[9] Suzuki, T.; Kunihara, K.; Kobayashi, M.; Tabata, S.; Higaki, K.; Ohnishi, H. A Micromachined Gas Sensor Based on a Catalytic Thick Film/SnO_2 Thin Film Bilayer and Thin Film Heater: Part 1: CH_4 Sensing. *Sens. Actuators B: Chem.* **2005**, *109*, 185-189.

[10] Tabata, S.; Higaki, K.; Ohnishi, H.; Suzuki, T.; Kunihara, K.; Kobayashi, M. A Micromachined Gas Sensor Based on a Catalytic Thick Film/SnO_2 Thin Film Bilayer and a Thin Film Heater: Part 2: CO Sensing. *Sens. Actuators B: Chem.* **2005**, *109*, 190-193.

[11] Suzuki, T.; Soma, S.; Nagase, T., Methane Sensor for Cordless Utility Gas Alarms. In FujiElectric Review, Fuji electric: 2012; Vol. 58, pp 37-40.

[12] Nonaka, A.; Nakajima, T.; Ohnishi, H.; Okamura, M.; Murata, N.; Suzuki, T. Realization of ultra low power consumption of SnO_2 Thin Film Gas Sensor. *Proc. the 57th Chem. Sensor Sym, Sup. B(Jpn)* **2014** *30* ,13-15.

[13] Koyayashi, M.; Yoshida, M.; Suzuki, T.; Kunihara, K.; Tabata, S.; Higaki, K.; Ohnishi, H.; Hashimoto, T. Thin Layer Sensor. Jpn. Patent JP4376093 2009.
[14] Suzuki, T.; Okamura, M.; Murata, N.; Nonaka, A.; Nakajima, T.; Ohnishi, H. Development for Practical Use of Battery Driven Gas Sensor. *Proc. The 57th Chem. Sensor Sym. Sup. B(Jpn)* **2014** *30* ,19-21.
[15] Fumi, U.; Suzuki, T.; Delaunay, J.-J., Gas Sensor. US Patent No. 9 910 023B2(2018).
[16] Yamazoe, N. New Approaches for Improving Semiconductor Gas Sensors. Sens. Actuators B **1991**, *5*, 7-19.
[17] Yamazoe, N.; Fuchigami, J.; Kishikawa,M.; Seiyama, T. Interactions of Tin Oxide Surface with O_2, H_2O and H_2. *Surf. Sci.* **1979**, 86, 335-344.
[18] Kocemba, I.; Rynkowski, J. The Influence of Catalytic Activity on the Response of Pt/SnO_2 Gas Sensors to Carbon Monoxide and Hydrogen. *Sens. Actuators B: Chem.* **2011**, *155*, 659-666.
[19] Gaidi, M.; Labeau, M.; Chenevier, B.; Hazemann, J. L. In-situ EXAFS Analysis of the Local Environment of Pt Particles Incorporated in Thin Films of SnO_2 Semi-Conductor Oxide used as Gas-Sensors. *Sens. Actuators B: Chem.* **1998**, *48*, 277-284.
[20] Mädler, L.; Sahm, T.; Gurlo, A.; Grunwaldt, J. -D.; Barsan, N.; Weimar, U.; Pratsinis, S. E. Sensing Low Concentrations of CO using Flame-Spray-Made Pt/SnO_2 Nanoparticles. *J. Nanoparticle Res.* **2006**, *8*, 783-796.
[21] Kowal, A.; Li, M.; Shao, M.; Sasaki, K.; Vukmirovic, M. B.; Zhang, J.; Marinkovic, N. S.; Liu, P.; Frenkel, A. I.; Adzic, R. R. Ternary Pt/Rh/SnO_2 Electrocatalysts for Oxidizing Ethanol to CO_2. *Nat. Mater.* **2009**, *8*, 325-330.
[22] Gaidi, M.; Hazemann, J. L.; Matko, I.; Chenevier, B.; Rumyantseva, M.; Gaskov, A.; Labeau, M. Role of Pt Aggregates in Pt/SnO_2 Thin Films used as Gas Sensors Investigations of the Catalytic Effect. *J. Electrochem. Soc.* **2000**, *147*, 3131-3138.
[23] Hübner, M.; Koziej, D.; Bauer, M.; Barsan, N.; Kvashnina, K.; Rossell, M. D.; Weimar, U.; Grunwaldt, J.-D. The Structure and Behavior of Platinum in SnO_2-Based Sensors under Working Conditions. *Angew. Chem. Int. Ed.* **2011**, 50, 2841-2844.
[24] Puigdollers, A. R.; Schlexer, P.; Tosoni, S.; Pacchioni, G. Increasing Oxide Reducibility: The Role of Metal/Oxide Interfaces in the Formation of Oxygen Vacancies. *ACS Catal.* **2017**, *7*, 6493-6513.
[25] Murata, N.; Suzuki, T.; Kobayashi, M.; Togoh, F.; Asakura, K. Characterization of Pt-Doped SnO_2 Catalyst for a High-Performance Micro Gas Sensor. *Phys. Chem. Chem. Phys.* **2013**, *15*, 17938-17946.
[26] Hübner, M.; Bârsan, N.; Weimar, U. Influences of Al, Pd and Pt Additives on the Conduction Mechanism as well as the Surface and Bulk Properties of SnO_2 Based Polycrystalline Thick Film Gas Sensors. *Sens. Actuators B* **2012**, *171-172*, 172-180.
[27] Degler, D.; Pereira de Carvalho, H.W.; Kvashnina, K.; Grunwaldt, J. -D.; Weimar, U.; Barsan, N. Structure and Chemistry of Surface-Doped Pt:SnO_2 Gas Sensing Materials. *RSC Adv.* **2016**, *6*, 28149-28155.
[28] Nishihata, Y.; Mizuki, J.; Akao, T.; Tanaka, H.; Uenishi, M.; Kimura, N.; Okamoto, T.; Hamada, N. Self-Regeneration of a Pd-Perovskite Catalyst for Automotive Emissions Control. *Nature* **2002**, 418, 164-167.
[29] Murata, N.; Kobayashi, M.; Okada, Y.; Suzuki, T.; Nitani, H.; Niwa, Y.; Abe, H.; Wada, T.; Mukai, S.; Uehara, H.; Ariga, H.; Takakusagi, S.; Asakura, K. A High-Temperature in situ Cell with a Large Solid Angle for Fluorescence X-Ray Absorption

Fine Structure Measurement. *Rev. Sci. Instrum.* **2015**, *86*, 034102.
[30] Nomura, M. Dead-Time Correction of a Multi-Element SSD for Fluorescent XAFS. *J.Synchrotron Rad.* **1998**, *5*, 851-853.
[31] Nomura, M.; Koyama, A. Design and Performance of a New XAFS Beamline at the Photon Factory; BL12C, in: KEK Report, Photon Factory, **1996**.
[32] Nomura, M.; Koike, Y.; Sato, M.; Koyama, A.; Inada, Y.; Asakura, K. A New XAFS Beamline NW10A at the Photon Factory. *AIP Conf. Proc.* **2007**, *882*, 896-898.
[33] Asakura, K. Analysis of EXAFS, *X-ray Absorption Fine Structure for Catalysts and Surfaces*, eds. Y. Iwasawa (World Scientific, Singapore, 1996) p. 33.
[34] Taguchi, T. REX2000 Version 2.5: Improved DATA Handling and Enhanced User-Interface. *AIP Conf. Proc.* **2007**, *882*, 162-164.
[35] Asakura, K. in: Catalysis, Vol. 24, eds. J. G. Catalano, 2012, p. 281.
[36] Cook, J. W.; Sayers, D. E. Criteria for Automatic X-Ray Absorption Fine Structure Background Removal. *J. Appl. Phys.* **1981**, *52*, 5024-5031.
[37] Newville, M.; Kas, J. J.; Rehr, J. J. Improvements in Modeling EXAFS with Many-Pole Self-Energy and FEFF 8.5. *J. Phys. Conf. Ser.* **2009**, *190*, 012023.
[38] Rehr, J. J.; Kas, J. J.; Prange, M. P.; Sorini, A. P.; Takimoto, Y.; Vila, F. Ab initio Theory and Calculations of X-ray Spectra. *Comptes Rendus Physique* **2009**, *10*, 548-559.
[39] Rehr, J. J. Theory and Calculations of X-ray Spectra: XAS, XES, XRS, and NRIXS. *Radiation Phys. Chem.* **2006**, *75*, 1547-1558.
[40] Hamilton, W. C. Significance Tests on the Crystallographic R Factor. *Acta Cryst.* **1965**, *18*, 502-510.
[41] Lee, P. A.; Beni, G. New Method for the Calculation of Atomic Phase Shifts: Application to Extended X-Ray Absorption Fine Structrue in Molecules and Crystals. *Phys. Rev. B* **1977**, 15, 2862-2883.
[42] Wada, T.; Murata, N.; Suzuki, T.; Uehara, H.; Nitani, H.; Niwa, Y.; Uo, M.; Asakura, K., Improvement of a Real Gas-Sensor for the Origin of Methane Selectivity Degradation by μ-XAFS Investigation. *Nano-Micro Lett.* **2015**, 7, 255-260.
[43] Wada, T.; Murata, N.; Uehara, H.; Suzuki, T.; Nitani, H.; Niwa, Y.; Uo, M.; Asakura, K., Degradation mechanism of a high-performance real micro gas sensor, as determined by spatially resolved XAFS. *Phys. Chem. Chem. Phys.* **2016**, 18, 7374-7380.
[44] Bartholomew, C. H. Mechanisms of Catalyst Deactivation. *Appl. Catal. A* **2001**, 212, 17-60.
[45] Forzatti, P.; Lietti, L. Catalyst Deactivation. *Catal. Today* **1999**, 52, 165-181.
[46] Takakusagi, S.; Kunimoto, A.; Sirisit, N.; Uehara, H.; Ohba, T.; Uemuara, Y.; Wada, T.; Ariga, H.; Chun, W.-J.; Iwasawa, Y.; Asakura, K. A New Indicator for Single Metal Dispersion on a TiO_2(110) Surface Premodified with a Mercapto Compound. *J. Phys. Chem. C.* **2016**, 120, 15785–15791.
[47] Liu, Q.; Zhang, Z. Platinum Single-Atom Catalysts: A Comparative Review towards Effective Characterization. *Catalysis Science & Technology* **2019**, 9, 4821-4834.
[48] Zhai, Y.; Pierre, D.; Si, R.; Deng, W.; Ferrin, P.; Nilekar, A. U.; Peng, G.; Herron, J. A.; Bell, D. C.; Saltsburg, H. Alkali-Stabilized Pt-OH_x Species Catalyze Low-

Temperature Water-Gas Shift Reactions. *Science* **2010**, 329, 1633-1636.
[49] Nie, L.; Mei, D.; Xiong, H.; Peng, B.; Ren, Z.; Hernandez, X. I. P.; Delariva, A.; Wang, M.; Engelhard, M. H.; Kovarik, L.; Datye, A. K.; Wang, Y. Activation of Surface Lattice Oxygen in Single-Atom Pt/CeO_2 for Low-Temperature CO Oxidation. *Science* **2017**, 358, 1419-1423.
[50] Jeong, H.; Shin, D.; Kim, B. S.; Bae, J.; Shin, S.; Choe, C.; Han, J. W.; Lee, H. Controlling the Oxidation State of Pt Single Atoms for Maximizing Catalytic Activity. *Angew. Chem.* **2020,** *132* (46), 20872-20877.
[51] Qiao, B.; Wang, A.; Yang, X.; Allard, L. F.; Jiang, Z.; Cui, Y.; Liu, J.; Li, J.; Zhang, T. Single-Atom Catalysis of CO Oxidation using Pt_1/FeO_x. *Nature Chemistry* **2011,** *3*, 634-641.
[52] Beppu, K.; Hosokawa, S.; Asakura, H.; Teramura, K.; Tanaka, T. Role of Lattice Oxygen and Oxygen Vacancy Sites in Platinum Group Metal Catalysts Supported on $Sr_3Fe_2O_{7-\delta}$ for NO-Selective Reduction. *Catal. Sci. Technol.* **2018**, *8*, 147-153.
[53] Asakura, K.; Nagahiro, H.; Ichikuni, N.; Iwasawa, Y. Structure and Catalytic Combustion Activity of Atomically Dispersed Pt Species at MgO Surface. *Appl. Catal. A,* **1999**, 188, 313-324.
[54] Zhang, C.; Liu, F.; Zhai, Y.; Ariga, H.; Yi, N.; Liu, Y.; Asakura, K.; Flytzani-stephanopoulos, M.; He, H. Alkali-Metal-Promoted Catalysis with Platinum / Titanium Dioxide for Formaldehyde Oxidation at Ambient Temperatures. *Angew. Chem., Int. Ed.* **2012**, 51, 1-6.
[55] Choi, C. H.; Kim, M.; Kwon, H. C.; Cho, S. J.; Yun, S.; Kim, H.-T.; Mayrhofer, K. J.; Kim, H.; Choi, M. Tuning Selectivity of Electrochemical Reactions by Atomically Dispersed Platinum Catalyst. *Nat. Commun.* **2016**, 7, 1-9.
[56] Liu, J.; Jiao, M.; Lu, L.; Barkholtz, H. M.; Li, Y.; Wang, Y.; Jiang, L.; Wu, Z.; Liu, D.-J.; Zhuang, L. High Performance Platinum Single Atom Electrocatalyst for Oxygen Reduction Reaction. *Nat. Commun.* **2017**, 8, 1-10.
[57] Li, H.; Wang, L.; Dai, Y.; Pu, Z.; Lao, Z.; Chen, Y.; Wang, M.; Zheng, X.; Zhu, J.; Zhang, W. Synergetic Interaction between Neighbouring Platinum Monomers in CO_2 Hydrogenation. *Nat. nanotech.* **2018**, 13, 411-417.
[58] Baidya, T.; Priolkar, K. R.; Sarode, P. R.; Hegde, M. S.; Asakura, K.; Tateno, G.; Koike, Y. Local Structure of Pt and Pd Ions in $Ce_{1-x}Ti_xO_2$: X-Ray Diffraction, X-Ray Photoelectron Spectroscopy, and Extended X-Ray Absorption Fine Structure. *J. Chem. Phys.* 2008, *128*, 124711.
[59] Chen, Y.; Ji, S.; Sun, W.; Chen, W.; Dong, J.; Wen, J.; Zhang, J.; Zheng, Z. Li, L.; Chen, C.; Peng, Q.; Wang, D.; Li, Y. Discovering Partially Charged Single-Atom Pt for Enhanced Anti-Markovnikov Alkene Hydrosilylation. *J. Am. Chem. Soc.* **2018**, 140, 7407-7410.
[60] Huang, H. H.; Wada, T.; Ariga, H.; Takakusagi, S.; Asakura, K.; Iwasawa, Y., Controlling the Inhomogeneity of Solid Catalysts at the Mesoscopic Scale. *Chem. Phys.Lett.* **2017**, 683, 18-21.

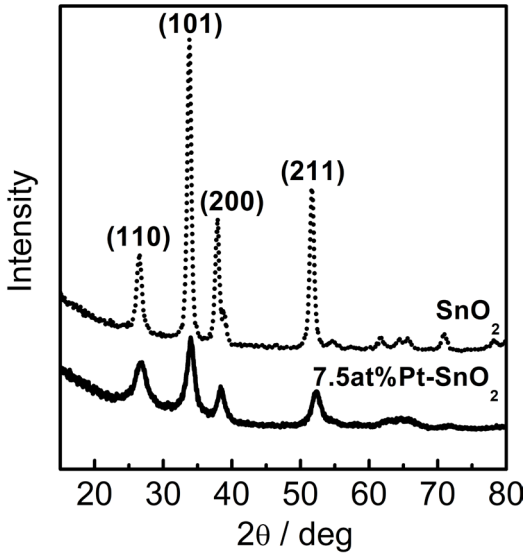

Figure 1. XRD spectra of SnO_2 and 7.5 at% Pt–SnO_2.

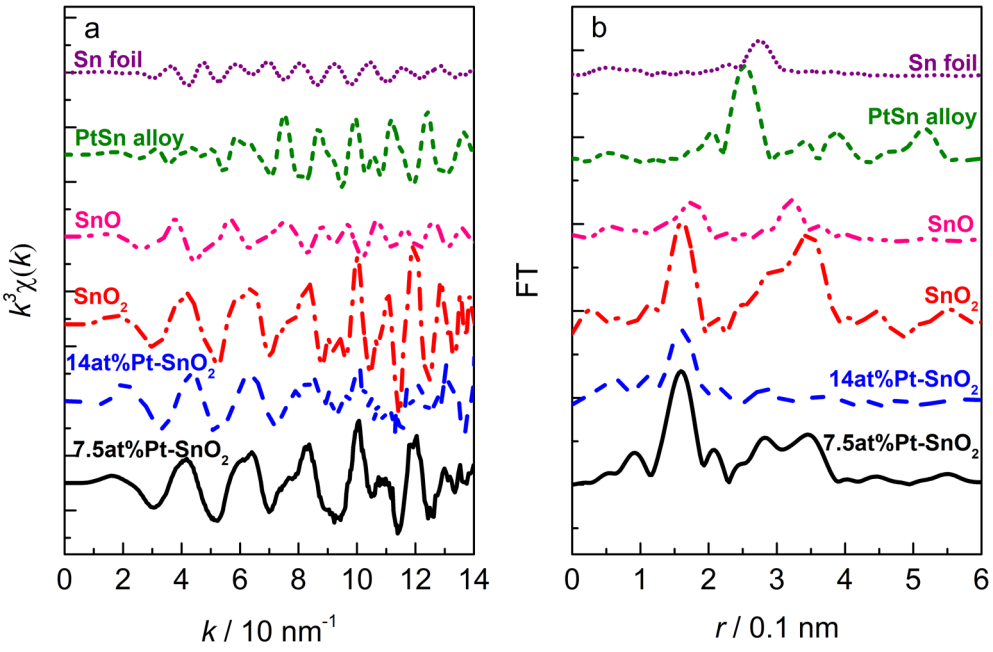

Figure 2. a: Sn K-edge k^3-weighted EXAFS oscillations ($k^3\chi$ (k)) and b: their Fourier transforms in dry air at RT for 7.5 at% and 14.0 at% Pt–SnO_2 together with those of reference compounds SnO_2, SnO, PtSn alloy (37 wt% Pt in alloy) and Sn-foil.

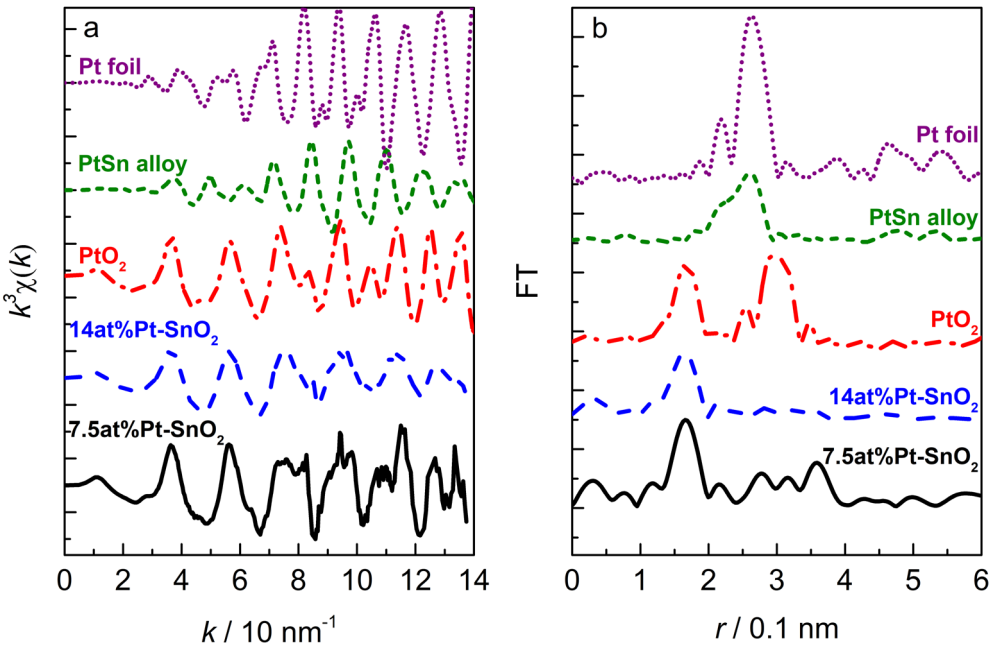

Figure 3. a: Pt L_3-edge k^3-weighted EXAFS oscillations ($k^3\chi(k)$) and b: their Fourier transforms in dry air at RT for 7.5 at% and 14.0 at% Pt–SnO_2 together with those of reference compounds PtO_2, PtSn alloy (37 wt% Pt in alloy) and Pt foil.

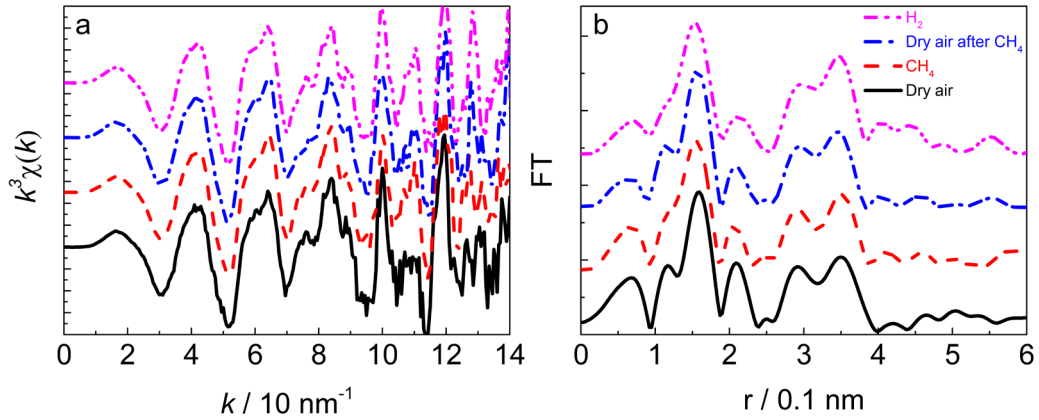

Figure 4. EXAFS for SnO_2 at 703 K. a: Sn K-edge k^3-weighted EXAFS oscillations ($k^3\chi$ (k)) and b: their Fourier transforms in dry air, CH_4, dry air after CH_4 and H_2.

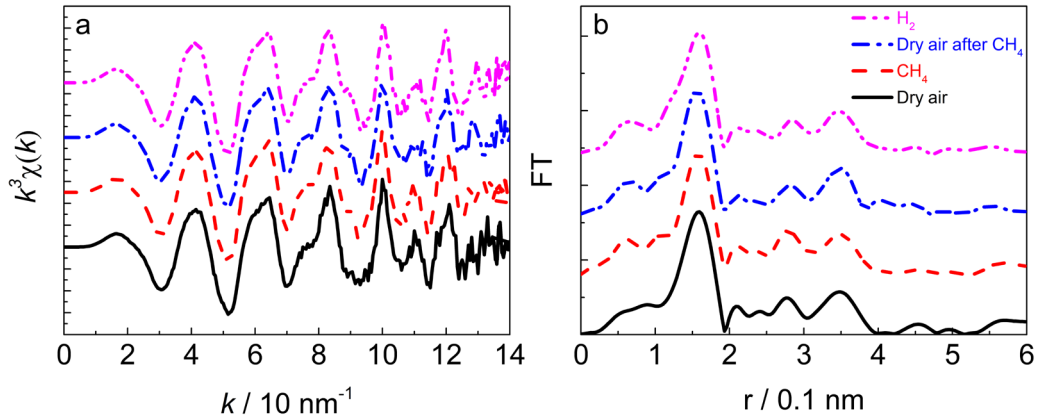

Figure 5. EXAFS for 7.5 at% Pt–SnO_2 at 703 K. a: Sn K-edge k^3-weighted EXAFS oscillations ($k^3\chi$ (k)) and b: their Fourier transforms in dry air, CH_4, dry air after CH_4 and H_2.

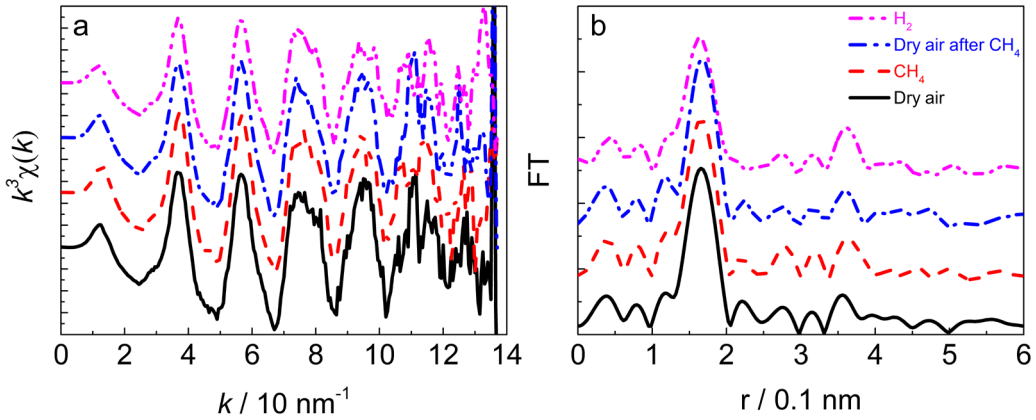

Figure 6. EXAFS for 7.5 at% Pt–SnO_2 at 703 K a: Pt L_3-edge k^3-weighted EXAFS oscillations ($k^3\chi$ (k)) and b: their Fourier transforms in dry air, CH_4, dry air after CH_4 and H_2.

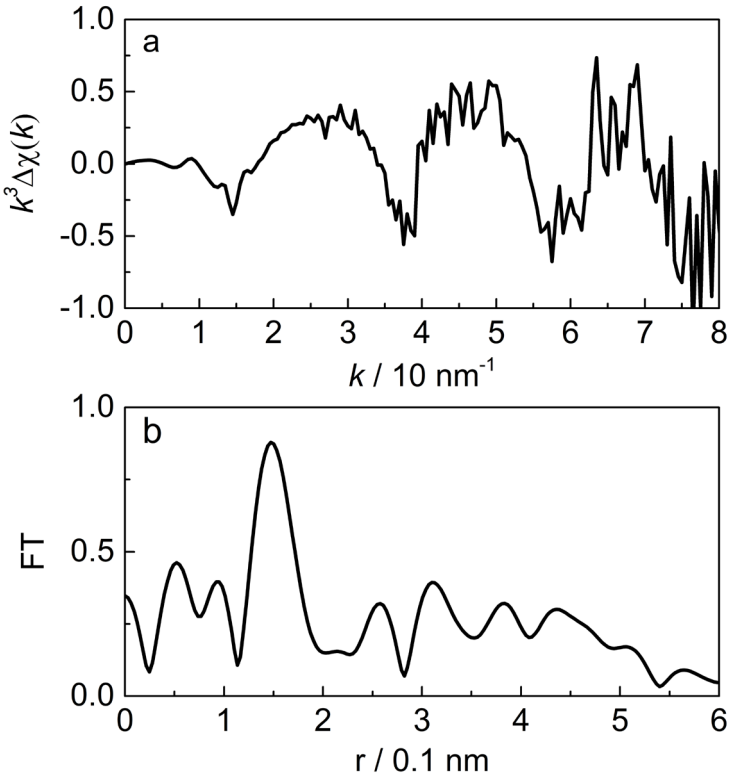

Figure 7. Difference spectra for Pt L_3-edge k^3-weighted EXAFS oscillations ($k^3\chi$ (k)) for 7.5 at% Pt–SnO_2. a: Difference before and after contact with H_2 at 703 K. b: Fourier transform of the difference.

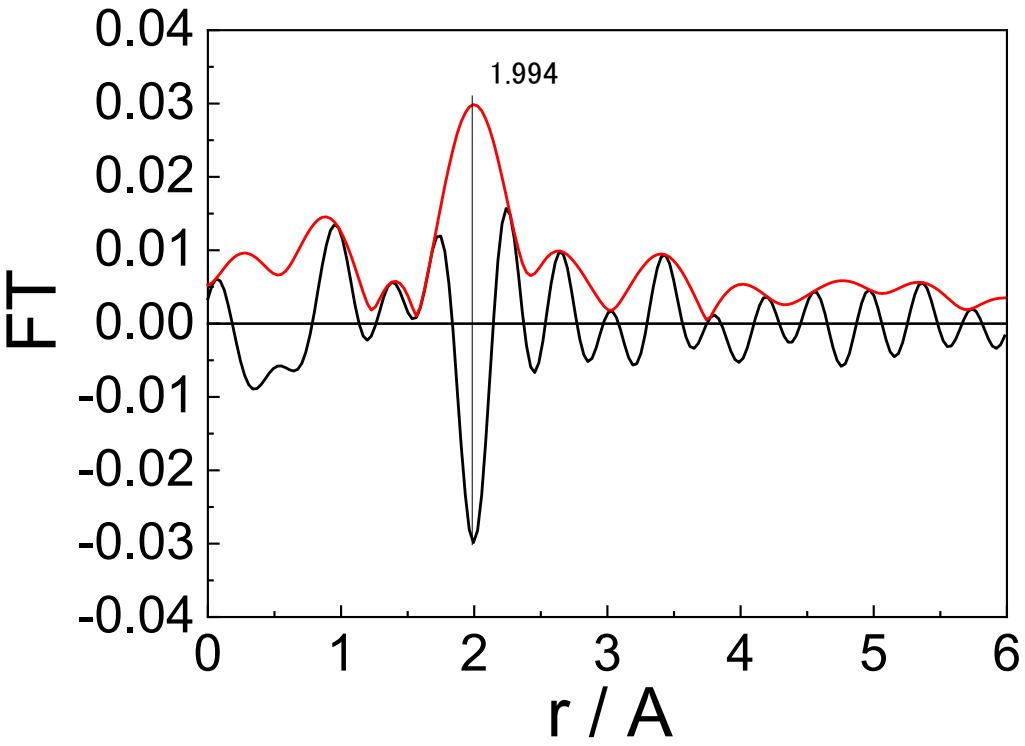

Figure 8. Imaginary (black) and absolute (red) parts of phase-corrected Fourier transform of difference spectrum of Pt–SnO_2 over the k range 2 – 9 Å.

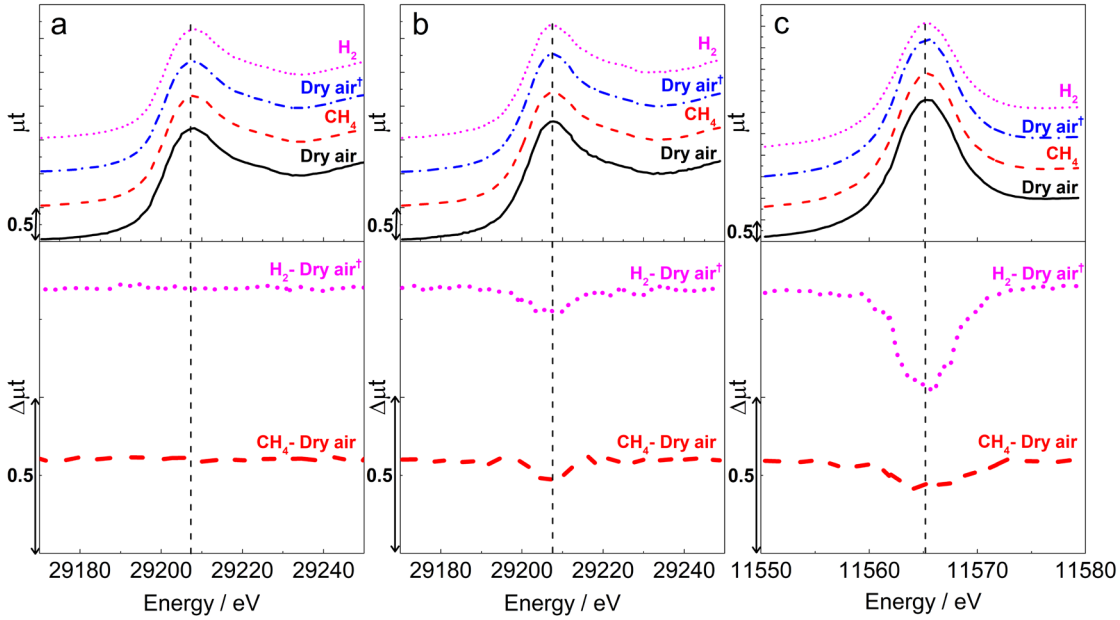

Figure 9. XANES of SnO_2 and 7.5 at% Pt–SnO_2 at 703 K. a: Sn K-edge of SnO_2, b: Sn K-edge, and c: Pt L_3-edge of Pt–SnO_2. Dry air† is air after CH_4 flow.

Table 1. Curve fitting results for Sn–O bond to Sn K-edge FT-EXAFS of SnO_2 using FEFF

Sn K-edge		Fitting results				
Gas	Temp. / K	*CN*	*r* / Å	ΔE / eV	σ^2 / Å^2	R / %
Dry air	303	6.0 ± 0.2	2.05 ± 0.01	28 ± 5	0.0049 ± 0.0007	2.8
	703	6.0 ± 0.3	2.05 ± 0.02	28 ± 5	0.0052 ± 0.0007	5.7
Methane	703	5.9 ± 0.4	2.05 ± 0.02	28 ± 5	0.0052 ± 0.0006	6.1
Hydrogen	703	5.9 ± 0.4	2.05 ± 0.02	28 ± 5	0.0053 ± 0.0007	6.9
Dry air	303	6.0 ± 0.4	2.05 ± 0.01	28 ± 5	0.0050 ± 0.0007	5.2

k range is $1.4 \leq k \leq 13.8$; r range is $1.3 \leq k \leq 1.9$; fitting space is back k space.

Table 2. Curve fitting results for Sn–O bond to Sn K-edge FT-EXAFS of Pt–SnO_2 using FEFF

Sn K-edge		Fitting results				
Gas	Temp. / K	*CN*	*r* / Å	ΔE / eV	σ^2 / Å^2	R / %
Dry air	303	6.0 ± 0.2	2.05 ± 0.01	28 ± 5	0.0046 ± 0.0007	2.9
	703	6.0 ± 0.3	2.05 ± 0.02	28 ± 5	0.0051 ± 0.0009	3.2
Methane	703	5.9 ± 0.4	2.05 ± 0.02	28 ± 5	0.0052 ± 0.0009	2.6
Hydrogen	703	5.9 ± 0.4	2.05 ± 0.02	28 ± 5	0.0053 ± 0.0009	3.3
Dry air	303	6.0 ± 0.4	2.05 ± 0.01	28 ± 5	0.0049 ± 0.0009	3.7

k range is $1.4 \leq k \leq 13.8$; r range is $1.3 \leq k \leq 1.9$; fitting space is back k space.

Table 3. Curve fitting results for Pt–O bond to Pt L_3-edge FT-EXAFS of Pt–SnO_2 using FEFF

Pt L_3-edge		Fitting results				
Gas	Temp. / K	*CN*	*r* / Å	ΔE / eV	σ^2 / Å^2	R / %
Dry air	303	6.0 ± 0.3	2.01 ± 0.02	28 ± 5	0.0042 ± 0.0006	3.8
	703	5.8 ± 0.4	2.01 ± 0.02	28 ± 5	0.0049 ± 0.0005	4.8
Methane	703	5.8 ± 0.4	2.01 ± 0.02	28 ± 5	0.0056 ± 0.0005	4.7
Hydrogen	703	5.3 ± 0.4	2.01 ± 0.02	28 ± 5	0.0064 ± 0.0004	3.4
Dry air	303	5.9 ± 0.3	2.01 ± 0.02	28 ± 5	0.0051 ± 0.0005	4/2

k range is $1.4 \leq k \leq 13.8$; r range is $1.3 \leq k \leq 1.9$; fitting space is back k space.

Table 4. Role and structure of Pt in Pt–SnO_2 in previous literature and this work

Pt state in/on SnO_2	Activating mechanism for sensing	Literature
Pt metallic nanoparticles	Spillover from Pt nanoparticles	16 - 18
Oxidized Pt nanoparticles	Spillover from oxidized Pt	7, 19 - 23
Metallic Pt nanoparticles	Redox reaction by lattice oxygen near Pt nanoparticles	24
Pt ions located at SnO_2 lattice sites, as low as 0.2 wt% Pt	Redox reaction by lattice oxygen near Pt atoms at the surface	18, 20, 26, 27
Pt ions located at SnO_2 lattice sites, as high as 29 wt% Pt	Creation of oxygen defects though Redox reaction by lattice oxygen near Pt atoms at surface, and diffusion through Pt–SnO_2 layer to SnO_2 sensor layer	This work, 25